nature

https://doi.org/10.1038/s41586-024-08525-3

Accelerated Article Preview

Signatures of ambient pressure superconductivity in thin film $La_3Ni_2O_7$

Received: 30 July 2024

Accepted: 12 December 2024

Accelerated Article Preview
Published online: 19 December 2024

Cite this article as: Ko, E. K. et al. Signatures of ambient pressure superconductivity in thin film $La_3Ni_2O_7$. *Nature* https://doi.org/10.1038/s41586-024-08525-3 (2024)

Eun Kyo Ko, Yijun Yu, Yidi Liu, Lopa Bhatt, Jiarui Li, Vivek Thampy, Cheng-Tai Kuo, Bai Yang Wang, Yonghun Lee, Kyuho Lee, Jun-Sik Lee, Berit H. Goodge, David A. Muller & Harold Y. Hwang

Signatures of ambient pressure superconductivity in thin film $La_3Ni_2O_7$

Eun Kyo Ko[1,2†*], Yijun Yu[1,2†*], Yidi Liu[1,3], Lopa Bhatt[4], Jiarui Li[1,2], Vivek Thampy[5], Cheng-Tai Kuo[5], Bai Yang Wang[1,3], Yonghun Lee[1,2], Kyuho Lee[1,3], Jun-Sik Lee[5], Berit H. Goodge[6], David A. Muller[4,7], and Harold Y. Hwang[1,2*]

[1]*Stanford Institute for Materials and Energy Sciences, SLAC National Accelerator Laboratory, Menlo Park, CA 94025, USA*

[2]*Department of Applied Physics, Stanford University, Stanford, CA 94305, USA*

[3]*Department of Physics, Stanford University, Stanford, CA 94305, USA*

[4]*School of Applied and Engineering Physics, Cornell University, Ithaca, New York 14850, USA*

[5]*Stanford Synchrotron Radiation Lightsource, SLAC National Accelerator Laboratory, Menlo Park, California 94025, USA*

[6]*Max Planck Institute for Chemical Physics of Solids, 01187 Dresden, Germany*

[7]*Kavli Institute at Cornell for Nanoscale Technology, Cornell University, Ithaca, New York 14850, USA*

[†]*These authors contributed equally to this work*

Recently, the bilayer nickelate $La_3Ni_2O_7$ has been discovered as a new superconductor with transition temperature T_c near 80 K under high pressure[1–3]. Despite extensive theoretical and experimental work to understand the nature of its superconductivity[4–29], the requirement of extreme pressure restricts the use of many experimental probes and limits its application potential. Here, we present signatures of superconductivity in $La_3Ni_2O_7$ thin films at ambient pressure, facilitated by the application of epitaxial compressive strain. The onset T_c varies approximately from 26 K to 42 K, with higher T_c values correlating with smaller in-plane lattice constants. We observed the co-existence of other Ruddlesden-Popper phases within the films and dependence of transport behavior with ozone annealing, suggesting that the observed low zero resistance T_c of around 2 K can be attributed to stacking defects, grain boundaries, and oxygen stoichiometry. This finding initiates numerous opportunities to stabilize and study superconductivity in bilayer nickelates at ambient pressure, and to

facilitate the broad understanding of the ever-growing number of high temperature and unconventional superconductors in the transition metal oxides.

Main

Since the discovery of high transition temperature (T_c) superconductivity in cuprates[30], the quest to discover layered oxides possessing electronic properties similar to those of cuprates has been of significant scientific interest[31–33]. In 2019, superconductivity was discovered in the infinite-layer nickelate via hole-doping the $3d^9$ (Ni^+) configuration[34], which shares related structural and *d*-electron characteristics with cuprate superconductors. Surprisingly, the bilayer nickelate $La_3Ni_2O_7$ (LNO_{327}), despite an electronic configuration of $3d^{7.5}$ ($Ni^{2.5+}$), was shown in 2023 to be a superconductor with a T_c near 80 K under high pressure (>14 GPa)[1–3]. This discovery sparked enormous theoretical research into the mechanism of superconductivity in LNO_{327} (Ref. [4–16]).

In contrast to the rapid theoretical developments, the requirement of extreme pressure has limited many experimental techniques to study the superconducting phase of LNO_{327} (Ref.[17–23]). Therefore, there is a strong drive to stabilize superconductivity at lower, or ideally, ambient pressure. Recognizing the key impact of the structural transitions induced under high pressure in LNO_{327} (Ref. [1,29]), several routes have been proposed to stabilize superconductivity at ambient pressure through "chemical" pressure via cation substitution or applying compressive strain[13–16]. While stabilizing the $A_3Ni_2O_7$ phase with cation substitution (such as A = Ba) is challenging[24], the strategy of applying epitaxial strain on LNO_{327} thin films appears promising[35–37], in analogy to T_c enhancements observed in cuprate thin films[38,39]. Here, we report evidence of superconductivity in LNO_{327} films at ambient pressure, achieved by applying compressive substrate strain.

Superconductivity of LNO_{327} films

We fabricated LNO_{327} films with varying strain states by depositing them on substrates having different in-plane lattice constants. The films were grown by pulsed laser deposition (PLD) (See methods for details) on $(LaAlO_3)_{0.3}(Sr_2TaAlO_6)_{0.7}$(001) [LSAT(001)], $LaAlO_3$(001) [LAO(001)], and $SrLaAlO_4$(001) [SLAO(001)] substrates, and the films were capped with 1 unit cell of $SrTiO_3$ (STO). The in-plane lattice constants for LSAT(001), LAO(001), and SLAO(001) substrates are 3.868 Å, 3.787 Å (pseudo-cubic), and 3.756 Å, respectively. Bulk LNO_{327} exhibits an orthorhombic *Amam* structure with a = 5.392 Å, b = 5.448 Å, and c = 20.5311 Å (Ref. [25]), giving

a pseudo-tetragonal in-plane lattice constant [$a_p = (a^2 + b^2)^{1/2}/2$] of 3.833 Å. **Figure 1a** shows x-ray diffraction (XRD) θ-2θ symmetric scans of the 5 nm-thick-films, showing the multiple (00l) diffraction peaks indexed to the LNO_{327} phase, along with substrates peaks. For LNO_{327} films grown on LSAT(001), LAO(001), and SLAO(001), the nominal in-plane misfit strain ($\varepsilon_{nominal}$) values are +0.9%, -1.2%, and -2.0%, respectively, assuming the LNO_{327} films are fully strained to the substrates. For convenience, we indicate compressive (tensile) strain with a minus (plus) sign.

According to previous bulk LNO_{327} studies[40,41], oxygen-deficient $LNO_{327-\delta}$ ($\delta > 0.08$) is insulating, while stoichiometric LNO_{327} is metallic. Note that all films in **Fig. 1** were annealed in ozone prior to the transport measurements (see methods for details). The as-grown LNO_{327} films before the ozone annealing are insulating (**Fig. 2a** and **Extended Data Fig. 1**). Ozone annealed LNO_{327} films on LSAT(001) and LAO(001) exhibit metallic behavior at high temperatures, with a resistive upturn below approximately 40 K and no signs of superconductivity (**Fig. 1b**). While transport properties show dramatic effects of ozone annealing, XRD exhibited little difference (**Extended Data Fig. 2**).

For the highest compressive strain, the ozone annealed LNO_{327} film on SLAO(001) (sample A1) exhibits a clear superconducting transition in the temperature-dependent resistivity $\rho(T)$ with onset T_c ($T_{c,\,onset}$) at 42.4 K, and zero resistance below 2.2 K (**Fig. 1b**). Additional samples (A12-14) exhibited zero resistance. To confirm that the superconducting transition is reproducible, we synthesized a number of additional films on SLAO(001) substrates (**Fig. 1c**). We observed a superconducting downturn in $\rho(T)$ in multiple samples, with $T_{c,\,onset}$ varying from 26.2 K to 42.4 K. To further confirm the presence of superconductivity, we performed two-coil mutual inductance measurements on a superconducting sample that reaches zero resistance (A12; **Extended Data Fig. 3**). A clear diamagnetic response was observed below zero resistance T_c, although the signal level is small due to the limited quality of the film.

Role of ozone annealing

To highlight the role of ozone annealing (See **Methods** and **Extended Data Fig. 4**), we show in **Fig 2a** that the film on SLAO(001) is insulating as grown, while after ozone annealing, the film is metallic above $T_{c,\,onset}$. We measured the time-evolution of $\rho(T)$ after ozone annealing on sample A1 (**Fig. 2b**). Just after annealing, the film shows a superconducting transition. After 8 and 20 days (stored in a desiccator), the film exhibits higher resistivity, but still shows traces of

superconductivity near a similar $T_{c,\,onset}$ to that of the film just after annealing. This indicates that the oxygen stoichiometry within the film is likely inhomogeneous, as reported in bulk LNO_{327} (Ref. [22]). After re-annealing the film with ozone, the superconducting transition and original resistivity were both recovered, illustrating the major role of reversible oxygen stoichiometry changes.

To study the effect of ozone annealing on the valence state of Ni, the Ni L_2-edge was investigated via x-ray absorption spectroscopy (XAS) before and after annealing for sample A1 using total electron-yield (TEY) detection (**Fig. 2c**). Given the nominal Ni valence of 2.5+ in LNO_{327}, both XAS spectra for LNO_{327} can be interpreted qualitatively as a mixed valence state of Ni^{2+} and Ni^{3+}. The XAS data before ozone treatment is consistent with a principal components fit of Ni^{2+}: 55% and Ni^{3+}: 45%. After ozone treatment, the best fit was Ni^{2+}: 50% and Ni^{3+}: 50%. This indicates that the Ni valence changed from ~2.45+ to ~2.5+ before and after ozone treatment, consistent with an increased oxidation state.

Transport properties

Figure 3a shows the temperature-dependent current-voltage measurements of sample A1. At 5 K, the current-voltage curves exhibit linear behavior and become increasingly nonlinear as the temperature decreases. The critical current density J_c at 150 mK is approximately 0.3 kA/cm^2, comparable to the bulk reported LNO_{327} value of 0.85 kA/cm^2 at 1.5 K and 16.6 GPa.[33] Notably, zero resistance or non-zero J_c shown here requires adequate filtering of external radiation (**Extended Data Fig. 5a, b**). Additionally, a detailed examination of the $\rho(T)$ curve reveals a two-step superconducting transition, which is frequently seen in Josephson-coupled superconducting domains (**Extended Data Fig. 5c**).

Next, we focus on the magnetic field response of superconductivity. **Figure 3b-c** display $\rho(T)$ plots of sample A1 with magnetic fields up to 14 T applied perpendicular and parallel to the *ab* plane, respectively. We estimate the upper critical fields ($H_{c,\perp}$ and $H_{c,||}$) based on $T_{c,\,90\%}$ (defined as the 90% of the resistance to the normal state near $T_{c,\,onset}$) to minimize the effect of inhomogeneity within the film. The extracted $H_{c,\perp}$ and $H_{c,||}$values are shown in **Fig. 3d**. We fit $H_{c,\perp}$ and $H_{c,||}$to the linearized Ginzburg-Landau form for a geometrically confined superconductor as

$$H_{c,\perp}(T) = \frac{\phi_0}{2\pi\xi_{ab}^2(0)}\left(1-\frac{T}{T_c}\right)$$

$$H_{c,||}(T) = \frac{\sqrt{12}\phi_0}{2\pi\xi_{ab}(0)d}\left(1-\frac{T}{T_c}\right)^{\frac{1}{2}},$$

where ϕ_0 is the flux quantum, $\xi_{ab}(0)$ is the zero-temperature Ginzburg-Landau coherence length, and d is the superconducting thickness[42]. We obtained $\xi_{ab}(0) \approx 1.8$ nm, which is comparable to that of bulk LNO_{327} (Ref. [3]). We found d to be approximately 5.0 ± 0.1 nm, which reasonably matches the thickness of the film determined by scanning transmission electron microscopy (STEM) measurements. The temperature-dependent Hall coefficient $R_H(T)$ is shown in **Extended Data Fig. 6**, and is characterized by a sign change at 200 K from negative at high temperatures, to positive at low temperature. This is consistent with a multiband electronic structure involving both electron and hole Fermi surfaces, observed in band structure calculations and by angle-resolved photoemission spectroscopy[17,21].

The relatively low value of J_c of LNO_{327} compared to infinite-layer nickelates ($J_c \approx 170$ kA/cm^2, Ref. [34]) or cuprates ($J_c \approx 1000$ kA/cm^2, Ref. [43]), the sensitivity of the zero-resistance state, and the observation of two-step transitions suggest that our films are characterized by weak links between superconducting puddles or domains that are limited by crystalline quality, or that the superconductivity has an interfacial or filamentary origin[26]. The close match between the measured thickness of the film with the derived superconducting thickness d suggests the former scenario, at least in the vertical direction.

Microscopic structure

To better understand the nature of superconductivity in the LNO_{327} films, we investigated the microscopic structure of sample A1 by STEM. **Figure 4a** shows an annular dark field (ADF)-STEM image along the [100] zone axis of the substrate. Occasional structural defects can be observed, leading to interruptions in the lateral connectivity of the LNO_{327} phase. **Figure 4b-d** display the enlarged ADF-STEM images of the regions indicated with solid white line boxes in **Fig. 4a**. The LNO_{327} film - substrate interface and LNO_{327} film - STO capping layer interface are indicated by white dashed lines. We marked the positions of La, Ni, Sr/La, and Al ions with colored circles. Region 1 (**Fig. 4b**) shows that the film consists of only the LNO_{327} phase, characterized by

a bilayer nickelate structure ($La_{n+1}Ni_nO_{3n+1}$, n = 2), which is highlighted in blue color. In contrast, region 2 and 3 (**Fig. 4c, d**) exhibit extended structural defects, which are indicated by yellow dashed line boxes. Notably, alongside the LNO_{327} phase, there is also the presence of the La_2NiO_4 (LNO_{214}) phase (n = 1), which is marked in red. According to several recent bulk studies, LNO_{327} can exhibit a complex stacking arrangement where single-layer (n = 1) and trilayer (n = 3) of NiO_6 octahedra alternate in a "1313" pattern[44–46]. However, we did not observe the specific "1313" phase across a number of STEM images taken in our LNO_{327} films.

To obtain further insight into the relationship between structural inhomogeneity and superconductivity, we roughly estimated the volume ratio of Ruddlesden-Popper (RP) phases ($La_{n+1}Ni_nO_{3n+1}$ (n = 1, 2, 3, …, ∞)) within the films by analyzing ADF-STEM images. We compared two samples, A1 and A4, both of which exhibit a superconducting downturn in $\rho(T)$. Sample A1 shows zero resistance, while sample A4 does not and has a high residual resistivity at 2 K (ρ(2 K) ≈ 0.2 mΩ·cm) (**Fig. 1c**). For sample A1, the film consists of LNO_{327} and LNO_{214}, while sample A4 contains not only the LNO_{327} and LNO_{214} phases but also the $La_4Ni_3O_{10}$ (LNO_{4310}) (n = 3) phase (**Extended Data Fig. 7**). The presence of LNO_{4310} or LNO_{214} phases leads to a reduction in the LNO_{327} ratio, which correlates with a broadened superconducting transition and the failure to reach zero resistance. While superconductivity was recently observed in bulk LNO_{4310} under high pressure[47], sample A1 does not appear to contain LNO_{4310} phase across several STEM images with a field of view of 10s of nm scale. Additionally, the lack of apparent LNO_{4310} Bragg peaks in the XRD scan serves as further evidence supporting superconductivity in our case originating from the compressively strained bilayer nickelate.

Correlation of structure and $T_{c,\,onset}$

To understand if there is a correlation between the lattice constants and $T_{c,\,onset}$ in LNO_{327} films, we extracted lattice constants from XRD results. In particular, the strain state of the film sample A1 was measured using synchrotron x-ray reciprocal space mapping (RSM) (**Extended Data Fig. 8**). The extracted in-plane lattice constant of LNO_{327} film is 3.77 Å, and the strain state of the film corresponds to in-plane misfit strain ε = -1.6%. **Extended Data Figures 8, 9** show XRD results of both representative superconducting and non-superconducting films. The in-plane and out-of-plane lattice constants are obtained from the (11$\underline{7}$) and (006) Bragg peaks of LNO_{327}, respectively.

We plotted the $T_{c,\,onset}$ versus lattice constant with references of the bulk LNO_{327} and $La_2PrNi_2O_7$ under high pressure (**Fig. 5a,b**)[1,27,28]. The relationship between the in-plane lattice constant and $T_{c,\,onset}$ is well-aligned between bulk samples under pressure and our thin films. The LNO_{327} films with smaller in-plane lattice constants have higher $T_{c,\,onset}$, and the LNO_{327} films with in-plane lattice constants larger than 3.79 Å did not exhibit a superconducting transition. This suggests that the short in-plane Ni-O bond length is crucial for achieving superconductivity in LNO_{327}. On the other hand, there seems to be an anticorrelation between $T_{c,\,onset}$ and the out-of-plane lattice constant. This is a natural outcome of the different strain response to hydrostatic pressure versus epitaxial strain. However, it does suggest that superconductivity is robust to a wider range of *c*-lattice constant than previously reported.

Challenges and outlook

Much like the bulk LNO_{327} system, it is apparent that a central focus of future thin film studies will be to understand and control stacking uniformity and defects. We have observed the onset of superconductivity with increasing epitaxial compressive strain. Furthermore, our experiments thus far indicate that LNO_{327} films with a higher apparent ratio of the LNO_{327} phase exhibits a higher $T_{c,\,onset}$ with zero resistance. In the thermodynamic phase diagram of RP nickelates, there is a narrow LNO_{327} growth window between that of LNO_{214} and LNO_{4310}. However, it is already clear from the aforementioned "1313" stacking that even bulk materials may be considerably more complex [44–46]. Thin film synthesis has even further opportunities to exploit the kinetics of growth, in addition to considerations of thermodynamic stability – we suspect that there is a complex interplay between kinetic, thermodynamic, and strain factors. For example, the formation of LNO_{214} and LNO_{4310} phases can lead to faster strain relaxation in the film, since bulk LNO_{214} and LNO_{4310} have larger in-plane lattice constants than that of LNO_{327} (a_p = 3.862 Å for LNO_{214} and a_p = 3.847 Å for LNO_{4310})[48]. Ultimately, we anticipate that the understanding and optimization of these competing factors will enable greater crystalline control, analogous to the progress recently made for infinite-layer nickelates and bulk LNO_{327}. This initial stabilization of ambient pressure superconductivity in LNO_{327} films should facilitate a wide range of scattering and spectroscopic studies of this new high-T_c superconductor, to address the underlying question as to why so many different *d*-electron configurations in layered nickel oxides are superconducting[1,34,47,49].

References

1. Sun, H. *et al.* Signatures of superconductivity near 80 K in a nickelate under high pressure. *Nature* **621**, 493–498 (2023).

2. Hou, J. *et al.* Emergence of high-temperature superconducting phase in pressurized $La_3Ni_2O_7$ crystals. *Chin. Phys. Lett.* **40**, 117302 (2023).

3. Zhang, Y. *et al.* High-temperature superconductivity with zero resistance and strange-metal behavior in $La_3Ni_2O_{7-\delta}$. *Nat. Phys.* **20**, 1269–1273 (2024).

4. Luo, Z., Hu, X., Wang, M., Wú, W. & Yao, D. X. Bilayer two-orbital model of $La_3Ni_2O_7$ under pressure. *Phys, Rev. Lett.* **131**, 126001 (2023).

5. Zhang, Y., Lin, L. F., Moreo, A. & Dagotto, E. Electronic structure, dimer physics, orbital-selective behavior, and magnetic tendencies in the bilayer nickelate superconductor $La_3Ni_2O_7$ under pressure. *Phys. Rev. B* **108**, L180510 (2023).

6. Christiansson, V., Petocchi, F. & Werner, P. Correlated electronic structure of $La_3Ni_2O_7$ under pressure. *Phys. Rev. Lett.* **131**, 206501 (2023).

7. Yang, Q. G., Wang, D. & Wang, Q. H. Possible s± -wave superconductivity in $La_3Ni_2O_7$. *Phys. Rev. B* **108**, L140505 (2023).

8. Yang, Y. F., Zhang, G. M. & Zhang, F. C. Interlayer valence bonds and two-component theory for high-T_c superconductivity of $La_3Ni_2O_7$ under pressure. *Phys. Rev. B* **108**, L201108 (2023).

9. Liu, Y. B., Mei, J. W., Ye, F., Chen, W. Q. & Yang, F. s±-wave pairing and the destructive role of apical-oxygen deficiencies in $La_3Ni_2O_7$ under pressure. *Phys. Rev. Lett.* **131**, 236002 (2023).

10. Shen, Y., Qin, M. & Zhang, G. M. Effective bi-layer model hamiltonian and density-matrix renormalization group study for the high-T_c superconductivity in $La_3Ni_2O_7$ under high pressure. *Chin. Phys. Lett.* **40**, 127401 (2023).

11. Lechermann, F., Gondolf, J., Bötzel, S. & Eremin, I. M. Electronic correlations and superconducting instability in $La_3Ni_2O_7$ under high pressure. *Phys. Rev. B* **108**, L201121 (2023).

12. Oh, H. & Zhang, Y. H. Type-II t-J model and shared superexchange coupling from Hund's rule in superconducting $La_3Ni_2O_7$. *Phys. Rev. B* **108**, 174511 (2023).

13. Rhodes, L. C. & Wahl, P. Structural routes to stabilize superconducting $La_3Ni_2O_7$ at ambient pressure. *Phys. Rev. Mater.* **8**, 044801 (2024).

14. Pan, Z., Lu, C., Yang, F. & Wu, C. Effect of rare-earth element substitution in superconducting $R_3Ni_2O_7$ under pressure. *Chin. Phys. Lett.* **41**, 087401 (2024).

15. Geisler, B., Hamlin, J. J., Stewart, G. R., Hennig, R. G. & Hirschfeld, P. J. Structural transitions, octahedral rotations, and electronic properties of $A_3Ni_2O_7$ rare-earth nickelates under high pressure. *npj Quantum Mater.* **9**, 38 (2024).

16. Sui, X. *et al.* Electronic properties of the bilayer nickelates $R_3Ni_2O_7$ with oxygen vacancies (R=La or Ce). *Phys. Rev. B* **109**, 205156 (2024).

17. Yang, J. *et al.* Orbital-dependent electron correlation in double-layer nickelate $La_3Ni_2O_7$. *Nat Commun* **15**, 4373 (2024).

18. Chen, K. *et al.* Evidence of spin density waves in $La_3Ni_2O_{7-\delta}$. *Phys Rev Lett* **132**, 256503 (2024).

19. Kakoi, M. *et al.* Multiband metallic ground state in multilayered nickelates $La_3Ni_2O_7$ and $La_4Ni_3O_{10}$ probed by 139La-NMR at ambient pressure. *J. Phys. Soc. Jpn.* **93**, 053702 (2024).

20. Takegami, D. *et al.* Absence of Ni2+/Ni3+ charge disproportionation and possible roles of O 2p holes in $La_3Ni_2O_{7-\delta}$ revealed by hard x-ray photoemission spectroscopy. *Phys Rev B* **109**, 125119 (2024).

21. Li, Y. *et al.* Electronic correlation and pseudogap-like behavior of high-temperature superconductor $La_3Ni_2O_7$. *Chin. Phys. Lett.* **41**, 087402 (2024).

22. Dong, Z. *et al.* Visualization of oxygen vacancies and self-doped ligand holes in $La_3Ni_2O_{7-\delta}$. *Nature* **630**, 847–851 (2024).

23. Chen, X. *et al.* Electronic and magnetic excitations in $La_3Ni_2O_7$. *Nature Commun.* **15**, 9597 (2024).

24. Aggarwal, L. & Božović, I. The quest for high-temperature superconductivity in nickelates under ambient pressure. *Materials* **17**, 2546 (2024).

25. Wang, G. *et al.* Pressure-induced superconductivity in polycrystalline $La_3Ni_2O_{7-\delta}$. *Phys. Rev. X* **14**, 011040 (2024).

26. Zhou, Y. *et al.* Investigations of key issues on the reproducibility of high-T_c superconductivity emerging from compressed $La_3Ni_2O_7$. *Preprint at https://doi.org/10.48550/arXiv.2311.12361* (2024).

27. Li, J. *et al.* Pressure-driven right-triangle shape superconductivity in bilayer nickelate $La_3Ni_2O_7$. *Preprint at https://doi.org/10.48550/arXiv.2404.11369* (2024).

28. Wang, N. *et al.* Bulk high-temperature superconductivity in pressurized tetragonal $La_2PrNi_2O_7$. *Nature* **634**, 579–584 (2024).

29. Wang, L. *et al.* Structure responsible for the superconducting state in $La_3Ni_2O_7$ at high-pressure and low-temperature conditions. *J. Am. Chem. Soc.* **146**, 7506–7514 (2024).

30. Bednorz, J. G. & Miiller, K. A. Condensed possible high T_c superconductivity in the Ba-La-Cu-O System. *Z. Phys. B* **64**, 189–193 (1986).

31. Maeno, Y. *et al.* Superconductivity in a layered perovskite without copper. *Nature* **372**, 532–534 (1994).

32. Anisimov, V. I., Bukhvalov, D. & Rice, T. M. Electronic structure of possible nickelate analogs to the cuprates. *Phys. Rev. B* **59**, 7901–7906 (1995).

33. Lee, K. W. & Pickett, W. E. Infinite-layer $LaNiO_2$: Ni^{1+} is not Cu^{2+}. *Phys. Rev. B* **70**, 165109 (2004).

34. Li, D. *et al.* Superconductivity in an infinite-layer nickelate. *Nature* **572**, 624–627 (2019).

35. Li, Z. *et al.* Epitaxial growth and electronic structure of Ruddlesden-Popper nickelates ($La_{n+1}Ni_nO_{3n+1}$, n = 1-5). *APL Mater.* **8**, 091112 (2020).

36. Cui, T. *et al.* Strain-mediated phase crossover in Ruddlesden–Popper nickelates. *Commun. Mater.* **5**, 32 (2024).

37. Liu, Y. *et al.* Growth and characterization of the $La_3Ni_2O_{7-\delta}$ thin films: dominant contribution of the d_{x2-y2} orbital at ambient pressure. *Preprint at https://doi.org/10.48550/arXiv.2406.08789* (2024).

38. J.-P., L. *et al.* Doubling the critical temperature of $La_{1.9}Sr_{0.1}CuO_4$ using epitaxial strain. *Nature* **394**, 453–456 (1998).

39. Bozovic, I., Logvenov, G., Belca, I., Narimbetov, B. & Sveklo, I. Epitaxial strain and superconductivity in $La_{2-x}Sr_xCuO_4$ thin films. *Phys. Rev. Lett.* **89**, 107001 (2002).

40. Taniguchi, S. *et al.* Transport, magnetic and thermal properties of $La_3Ni_2O_{7-\delta}$. *J. Phys. Soc. Jpn.* **64**, 1644–1650 (1995).

41. Zhang, Z., Greenblatt, M. & Goodenough, J. B. Synthesis, structure, and properties of the layered perovskite $La_3Ni_2O_{7-\delta}$. *J. Solid State Chem.* **108**, 402–409 (1994).

42. Harper, F. E. & Tinkham, M. The mixed state in superconducting thin films. *Phys. Rev.* **172**, 441–450 (1968).

43. Smith, J. A., Cima, M. J. & Sonnenberg, N. High critical current density thick MOD-derived YBCO films. *IEEE Trans. Appl. Supercon.* **9**, 1531–1534 (1999).

44. Puphal, P. *et al.* Unconventional crystal structure of the high-pressure superconductor $La_3Ni_2O_7$. *Phys. Rev. Lett.* **133**, 146002 (2024).

45. Chen, X. *et al.* Polymorphism in the Ruddlesden-Popper nickelate $La_3Ni_2O_7$: discovery of a hidden phase with distinctive layer stacking. *J. Am. Chem. Soc.* **146**, 3640–3645 (2024).

46. Wang, H., Chen, L., Rutherford, A., Zhou, H. & Xie, W. Long-range structural order in a hidden phase of Ruddlesden-Popper bilayer nickelate $La_3Ni_2O_7$. *Inorg. Chem.* **63**, 5020–5026 (2024).

47. Zhu, Y. *et al.* Superconductivity in pressurized trilayer $La_4Ni_3O_{10-\delta}$ single crystals. *Nature* **631**, 531–536 (2024).

48. Song, J., Ning, D., Boukamp, B., Bassat, J. M. & Bouwmeester, H. J. M. Structure, electrical conductivity and oxygen transport properties of Ruddlesden-Popper phases $Ln_{N+1}Ni_nO_{3n+1}$ (Ln = La, Pr and Nd; N = 1, 2 and 3). *J. Mater. Chem. A* **8**, 22206–22221 (2020).

49. Pan, G. A. *et al.* Superconductivity in a quintuple-layer square-planar nickelate. *Nat. Mater.* **21**, 160–164 (2022).

Main Figure Legends

Figure 1 | Structural and electrical characterization of LNO_{327} films on various substrates. a, XRD θ-2θ symmetric scans of ozone-annealed LNO_{327} films on LSAT(001) (blue), LAO(001) (green), and SLAO(001) (red) substrates. The film on SLAO(001) was measured via synchrotron x-ray. Diffraction peaks of LNO_{327} are indicated with (00*l*). Diffraction peaks of LSAT(001), LAO(001), and SLAO(001) substrates are indicated with *, #, and ♦, respectively. **b**, Resistivity versus temperature $\rho(T)$ plots of the ozone-annealed LNO_{327} films. Zero resistance is observed in several samples, A1 and A12-14. **c**, $\rho(T)$ plots of a number of ozone-annealed LNO_{327} films grown on SLAO(001).

Figure 2 | Role of ozone annealing. a, $\rho(T)$ plots of LNO_{327} grown on SLAO(001) before and after ozone annealing. **b**, Time-dependent $\rho(T)$ plots of LNO_{327} films after ozone annealing. The vertical dashed line indicates $T_{c,\,onset}$. **c**, Ni *L*$_2$*-edge* XAS of LNO_{327} films before and after ozone annealing. The red (blue) solid line shows the result of Ni^{2+}:55 % and Ni^{3+}: 45% (Ni^{2+}:50 % and Ni^{3+}: 50%) combinations of the calculated reference spectra (purple and green dashed lines for Ni^{2+} and Ni^{3+}, respectively).

Figure 3 | Transport properties of LNO_{327} on SLAO(001). a, Electric field (*E*) versus current density (*J*) curves at various temperatures. The inset graph shows the temperature dependent

critical current density J_c. **b-c**, $\rho(T)$ under various magnetic fields applied perpendicular (**b**) and parallel (**c**) to the *ab* plane. **d**, Solid circles represent the upper critical fields ($H_{c,\perp}^{90\%}$ and $H_{c,||}^{90\%}$) extracted by the $T_{c,\,90\%}$. Solid lines are Ginzburg-Landau fits.

Figure 4 | Microscopic structure of the LNO_{327} film. a, ADF-STEM image of LNO_{327} on SLAO(001) along the [100] zone axis of the substrate. **b-d**, Enlarged ADF-STEM images for regions 1, 2, and 3, respectively, which are indicated with solid white line boxes in **Fig. 4a**. Extended structural defects are indicated by yellow dashed lines.

Figure 5 | $T_{c,\,onset}$ versus lattice constants. a-b, $T_{c,\,onset}$ versus in-plane and out-of-plane lattice constants, respectively. The bulk LNO_{327} and $La_2PrNi_2O_7$ results under high pressure from Refs.[1,27,28] are plotted for comparison.

Methods

Sample preparation

Polycrystalline $La_3Ni_2O_7$ (**Extended Data Fig. 10a**) and single crystalline $SrTiO_3$ were used as targets during the deposition process. The polycrystalline $La_3Ni_2O_7$ target was synthesized from La_2O_3 and NiO powder, sintered 4 times: 1000 °C for 12 hours, 1100 °C for 48 hours, 1100 °C for 24 hours, and 1200 °C for 24 hours. The $La_3Ni_2O_7$ and $SrTiO_3$ films were deposited by pulsed laser deposition with a KrF excimer laser (wavelength of 248 nm). Guided by the growth phase diagram of bulk $La_{n+1}Ni_nO_{3n+1}$ (**Extended Data Fig. 10b**)[50,51], we first obtained LNO_{214}, LNO_{327} and LNO_{113} by varying oxygen pressure and substrate temperature (**Extended Data Fig. 10c, d**). During the $La_3Ni_2O_7$ and $SrTiO_3$ film growth, the substrate temperature was maintained at 740 °C and 620 °C, respectively, under oxygen partial pressure $P(O_2)$ of 100 mTorr. The pulse laser repetition rate during the deposition was 5 Hz for $La_3Ni_2O_7$, and 2 Hz for $SrTiO_3$. The laser fluence was 0.3 J/cm^2 with a spot size of 5.1 mm^2. The $SrLaAlO_4$(001) substrates (MTI Corporation) were sonicated in acetone and IPA for 1 minute each. The films were annealed in a Samco UV1 ozone cleaner at 300 °C for ~2 hours at ambient pressure. Pure oxygen gas was supplied at a flow rate of 500 sccm, producing an ozone concentration of approximately ~0.4 wt% at room temperature. We note that the combination of low ozone concentration and suitable annealing temperature is critical,

as pure oxygen annealing at 1 atm does not induce metallic behavior in the films, while a high ozone concentration destabilizes the the LNO_{327} phase (**Extended Data Fig. 4**).

XRD measurements

The synchrotron XRD experiments were performed at room temperature at the Stanford Synchrotron Radiation Lightsource (SSRL) Beamline 17-2 with the photon energy of 15.0 keV or 8.3 keV. Laboratory XRD data were measured using a monochromated Cu $K_{\alpha 1}$ source ($\lambda = 1.5406$ Å). All XRD plots have been recalculated and plotted based on $\lambda = 1.5406$ Å.

STEM measurements

To prepare cross-sectional lamellas, we used a standard focused ion beam (FIB) lift-out procedure using a Thermo Fisher Helios G4 UX FIB. We performed STEM imaging in ADF mode using a Cs-corrected Thermo Fisher Scientific (TFS) Spectra 300 X-CFEG 300 kV with a probe convergence semi-angle of 30 mrad. Inner/outer collection angles in ADF geometry were 49/200.

Transport and mutual inductance measurements

25 nm thick Au electrodes were deposited using electron beam evaporation and then electrodes were bonded to sample holders with aluminum wires by an ultrasonic wire bonder. Magnetotransport measurements were performed using ^{4}He and dilution fridge cryostats. Home-made low-pass resistor–capacitor filters with cut-off frequency ~ 100 kHz were used. The same setup as in Ref. [52] was used to perform 2-coil mutual inductance measurements of the LNO_{327} films.

XAS measurements

XAS experiments were carried out at $T = 13.5$ K at Beamline 13-3 of the Stanford Synchrotron Radiation Lightsource (SSRL). The absorption spectra were acquired in total electron yield (TEY) mode. The incident x-rays were aligned parallel to the film's normal, with polarization set to $E//a$ (or b). XAS spectra were interpreted qualitatively as a mixed valence state of Ni^{2+} and Ni^{3+} (Ref. [23,53], and principal component analysis was performed to fit the contributions of Ni^{2+} and Ni^{3+} in samples before and after ozone annealing, respectively.

Methods References

50. Zinkevich, M., Solak, N., Nitsche, H., Ahrens, M. & Aldinger, F. Stability and thermodynamic functions of lanthanum nickelates. *J. Alloys Comp.* **438**, 92–99 (2007).

51. Zhang, J. et al. High oxygen pressure floating zone growth and crystal structure of the metallic nickelates $R_4Ni_3O_{10}$ (R=La,Pr). *Phys. Rev. Mater.* **4**, 083402 (2020).

52. Harvey, S. P. *et al.* Evidence for nodal superconductivity in infinite-layer nickelates. *Preprint at https://doi.org/10.48550/arXiv.2201.12971 (2022).*

53. Wang, L. *et al.* Spontaneous phase segregation of Sr_2NiO_3 and $SrNi_2O_3$ during $SrNiO_3$ heteroepitaxy. *Sci. Adv.* **7**, eabe2866 (2021).

54. Bøttcher, C. G. L. *et al.* Superconducting, insulating and anomalous metallic regimes in a gated two-dimensional semiconductor–superconductor array. *Nat. Phys.* **14**, 1138–1144 (2018).

55. Allain, A., Han, Z. & Bouchiat, V. Electrical control of the superconducting-to-insulating transition in graphene-metal hybrids. *Nat. Mater.* **11**, 590–594 (2012).

56. Chen, Z. *et al.* Carrier density and disorder tuned superconductor-metal transition in a two-dimensional electron system. *Nat. Commun.* **9**, 4008 (2018).

57. Eley, S., Gopalakrishnan, S., Goldbart, P. M. & Mason, N. Approaching zero-temperature metallic states in mesoscopic superconductor-normal-superconductor arrays. *Nat. Phys.* **8**, 59–62 (2012).

58. Gates-Rector, S. & Blanton, T. The powder diffraction file: a quality materials characterization database. *Powder Diffr.* **34**, 352–360 (2019).

Acknowledgments

We thank Y. Cui, T. P. Devereaux, S. A. Kivelson, R. B. Laughlin, W.-S. Lee, Yu Lin, Wendy Mao, S. Raghu, Z.-X. Shen and K.-J. Xu for discussions and assistance. This work was supported by the U. S. Department of Energy, Office of Basic Energy Sciences, Division of Materials Sciences and Engineering (Contract No. DE-AC02-76SF00515) and the Gordon and Betty Moore Foundation's Emergent Phenomena in Quantum Systems Initiative (grant no. GBMF9072, synthesis equipment). A part of this work was conducted at the Stanford Nano Shared Facilities

(SNSF), supported by the National Science Foundation under grant ECCS-1542152. The STEM measurements were performed at the Cornell Center for Materials Research Facilities supported by National Science Foundation (DMR-1719875). The microscopy work at Cornell was supported by the NSF PARADIM (DMR-2039380), with additional support from Cornell University, the Weill Institute and the Kavli Institute at Cornell. X-ray measurements were carried out at the SSRL, SLAC National Accelerator Laboratory, supported by the U.S. Department of Energy, Office of Science, Office of Basic Energy Sciences (Contract No. DE-AC02-76SF00515). Additional support (BHG) was provided by the Max Planck Society and Schmidt Science Fellows in partnership with the Rhodes Trust.

Author information

Author notes

1. These authors contributed equally: Eun Kyo Ko, Yijun Yu.

Authors and Affiliations

1. **Stanford Institute for Materials and Energy Sciences, SLAC National Accelerator Laboratory, Menlo Park, CA 94025, USA**
   Eun Kyo Ko, Yijun Yu, Yidi Liu, Jiarui Li, Bai Yang Wang, Yonghun Lee, Kyuho Lee, Harold Y. Hwang
2. **Department of Applied Physics, Stanford University, Stanford, CA 94305, USA**
   Eun Kyo Ko, Yijun Yu, Jiarui Li, Yonghun Lee, Harold Y. Hwang
3. **Department of Physics, Stanford University, Stanford, CA 94305, USA**
   Yidi Liu, Bai Yang Wang, Kyuho Lee
4. **School of Applied and Engineering Physics, Cornell University, Ithaca, New York 14850, USA**
   Lopa Bhatt, David A. Muller
5. **Stanford Synchrotron Radiation Lightsource, SLAC National Accelerator Laboratory, Menlo Park, California 94025, USA**
   Vivek Thampy, Cheng-Tai Kuo, Jun-Sik Lee
6. **Max Planck Institute for Chemical Physics of Solids, 01187 Dresden, Germany**

Berit H. Goodge

7. **Kavli Institute at Cornell for Nanoscale Technology, Cornell University, Ithaca, New York 14850, USA**

David A. Muller

Contributions

E.K.K. and Y.Y. contributed equally to this work. E.K.K. and H.Y.H. conceived and designed the project. E.K.K. and Y.Liu fabricated the films with input from K.L. Y.Y., E.K.K. and Y.Liu studied ozone annealing effects. Y.Y., E.K.K., Y.Liu and Y.Lee characterized the transport properties of films. L.B., B. H. G., D.A.M. measured and analyzed STEM images. E.K.K., Y.Liu, J.L., and V.T. performed XRD measurements. C.-T.K. and J.-S.L. contributed to the measurement and analysis of XAS. Y.Y. and B.Y.W. performed mutual inductance measurements. E.K.K., Y.Y. and H.Y.H. wrote the manuscript with contributions from all authors.

Corresponding author

Correspondence to Eun Kyo Ko (eunkyoko@stanford.edu), Yijun Yu (yuyijun@stanford.edu), or Harold Y. Hwang (hyhwang@stanford.edu)

Competing financial interests

No author has any competing financial interests.

Data availability

The source data presented in the figures are provided with this paper. Any additional data that support the findings of this study are available from the corresponding authors upon reasonable request.

Extended Data Figure Captions

Extended Data Fig. 1 | $\rho(T)$ plots of LNO_{327} grown on LSAT(001) (blue), LAO(001) (green), and SLAO(001) (red) before ozone annealing.

Extended Data Fig. 2 | Structural characterization of the LNO_{327} films before and after ozone annealing. a-c, XRD θ-2θ symmetric scans of LNO_{327} films on LSAT(001) (**a**), LAO(001) (**b**), and SLAO(001) (**c**) substrates before (red) and after (blue) ozone annealing. The scans of film on SLAO(001) were measured with synchrotron x-ray. Diffraction peaks of LNO_{327} are indicated with (00*l*). Diffraction peaks of LSAT(001), LAO(001), and SLAO(001) substrates are indicated with *, #, and ♦, respectively.

Extended Data Fig. 3 | Diamagnetic response of a superconducting LNO_{327} film (sample A12). **a**, The raw resistance as a function of temperature at zero field (red) and 2 T (purple). Inset shows the resistance evolution across a wider temperature range. **b**, **c**, The real (Re(V_p)) and imaginary (Im(V_p)) components of the voltage in the pickup coil, measured as a function of temperature using two-coil mutual inductance. The drive coil current was set to 0.05 mA. **d**, **e**, Re(V_p) and Im(V_p) as a function of temperature with different drive currents. Increasing drive current diminishes the screening response. **f**, **g**, Re(V_p) and Im(V_p) as a function of temperature under different magnetic fields. As the magnetic field increases, the onset of diamagnetic responses shifts to lower temperatures.

Extended Data Fig. 4 | Effect of oxygen and high concentration ozone annealing. **a**, Transport properties of a sample first annealed in O_2 and then annealed in nominally 0.4 wt% O_3. **b**, Transport properties of a sample first annealed in nominally 0.4 wt% O_3 and then annealed in O_2. **c**, XRD scans of the as-grown film and the film after ozone annealing at higher ozone concentration (15 wt%). The LNO_{327} phase disappears, and the LNO_{113} phase emerges.

Extended Data Fig. 5 | Fragility of the superconducting state in LNO_{327} film (sample A1). a, Resistance versus temperature $R(T)$ plots with and without filtering. **b,** Current-voltage curves at $T = 0.14$ K with and without filtering. These measurements used different electrode configurations compared to the those used in the main figures. **c,** A two-step transition in $R(T)$ plot**.** Such two-step transitions are commonly observed in Josephson-coupled superconducting regions[54–57]. Here the definition of $T_{c,\,onset}$ follows the main text. $T_{c,\,0}$ is zero resistance T_c. T_F is defined as the characteristic temperature of phase fluctuating regions as defined in Ref. [56].

Extended Data Fig. 6 | Hall coefficient (R_H) as a function of temperature for LNO_{327} film (sample A1). a, Hall resistance (R_{xy}) versus magnetic field applied perpendicular to the *ab* plane. **b,** Temperature dependent R_H. The vertical dashed line indicates $T_{c,\,onset}$.

Extended Data Fig. 7 | The estimated volume ratio of RP phases in LNO_{327} films. **a,** $\rho(T)/\rho(200\ K)$ plots of samples A1 and A4. **b,** Estimated fraction of LNO_{4310}, LNO_{327}, LNO_{214} in sample A1 and A4, analyzed from STEM images. This estimate does not consider projection effects of the finite cross-section, the immediate interface region between the film and substrate (i.e. up to the first LaO layer), and extended structural defects which cannot be projected to an RP phase. The estimates are based on multiple images of 10s of nm field of view. **c,** Representative ADF-STEM images of sample A4.

Extended Data Fig. 8 | Transport and structural properties for films with superconducting downturns (samples A1, A6) and without the downturns (sample B1, B2) in $\rho(T)$. a, b, $\rho(T)$ and $\rho(T)/\rho(200\ K)$ plots for samples A1, A6, B1, and B2. For samples A1, A6, and B1, films were grown on SLAO(001), and for sample B2, the film was grown on LSAT(001). **c-e,** Synchrotron x-ray RSM of the films on SLAO(001) (samples A1 (**c**), A6 (**d**), and B1 (**e**)). The (11$\underline{7}$) Bragg peaks of LNO_{327} are measured along with the (10$\underline{11}$) Bragg peaks of SLAO(001). **f,** RSM of a LNO_{327} film on LSAT(001). The (11$\underline{7}$) Bragg peak of LNO_{327} is measured along with the (103) Bragg peak of LSAT(001). The dashed circles indicate the Bragg peaks of LNO_{327} films.

Extended Data Fig. 9 | Structural and electrical properties of ozone-annealed LNO_{327} films on SLAO(001). a,b, XRD θ-2θ symmetric scans for superconducting samples (A1-A12) (**a**), and non-superconducting samples (B1, B3-B6) (**b**) near the (006) diffraction peak of LNO_{327}; the (004) diffraction peak of the SLAO(001) substrate is denoted by ♦. The scans for samples A1, A5, and A6 are measured with synchrotron x-rays. **c,** $\rho(T)$ plots for the non-superconducting samples.

Extended Data Fig. 10 | Growth phase diagram of $La_{n+1}Ni_nO_{3n+1}$. **a**, XRD θ-2θ symmetric scan for polycrystalline LNO_{327} target with a reference powder diffraction file (PDF 00-050-0244)[58]. The density of the LNO_{327} target is approximately 60% single crystal density. **b**, Phase diagram of $La_{n+1}Ni_nO_{3n+1}$ replotted from Ref. [50]. **c**, Phase diagram obtained by our experiments. **d**, XRD of as-grown $La_{n+1}Ni_nO_{3n+1}$ thin films under various conditions.

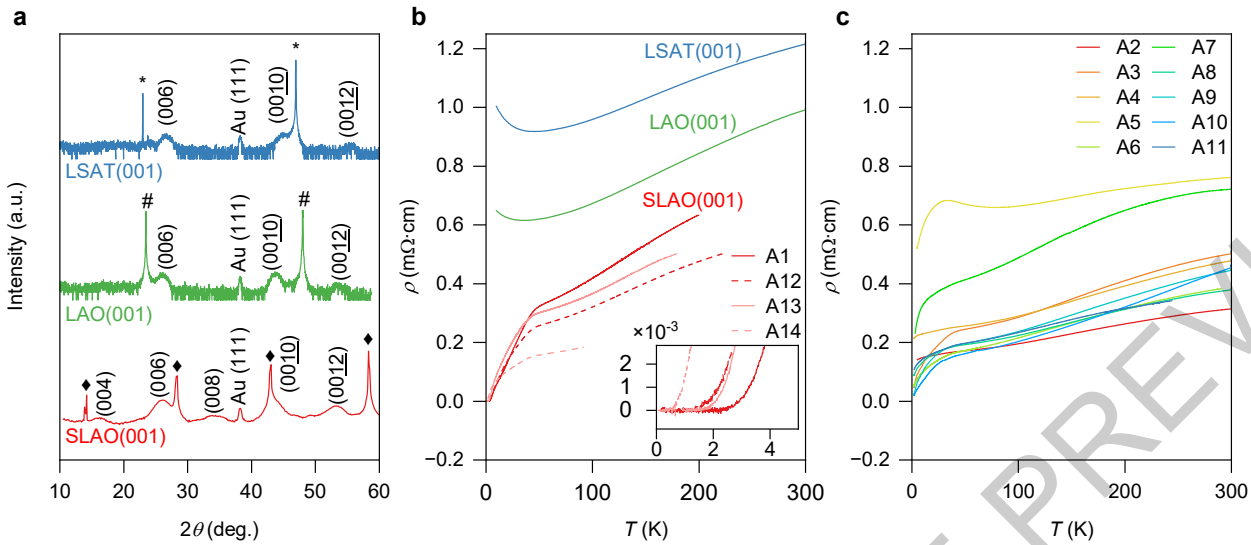

Figure 1, *E. K. Ko et al.*

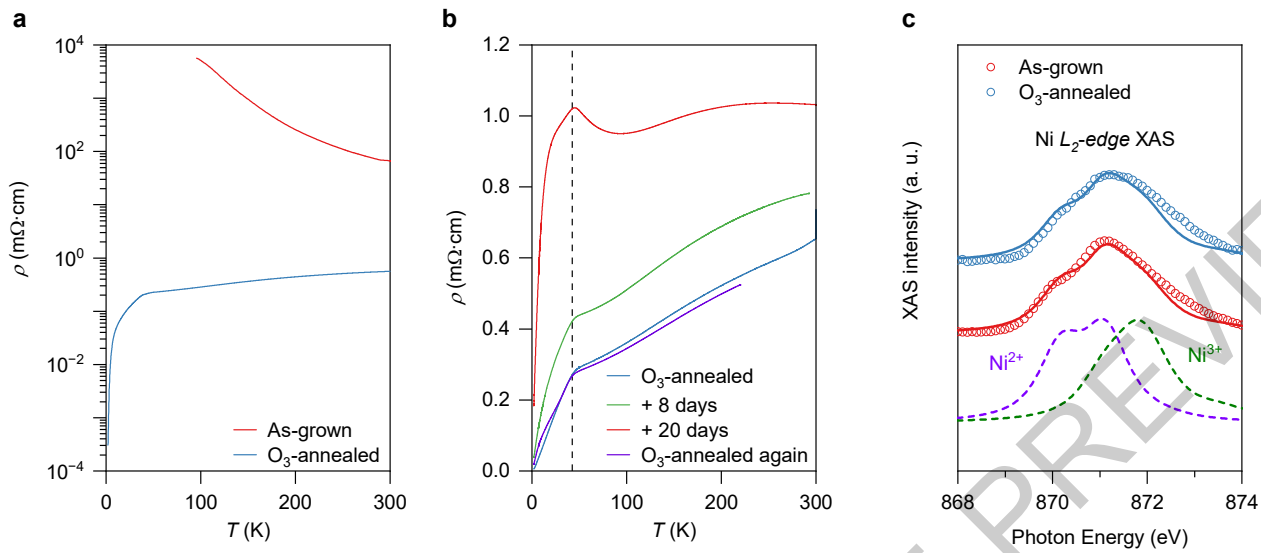

Figure 2, *E. K. Ko et al.*

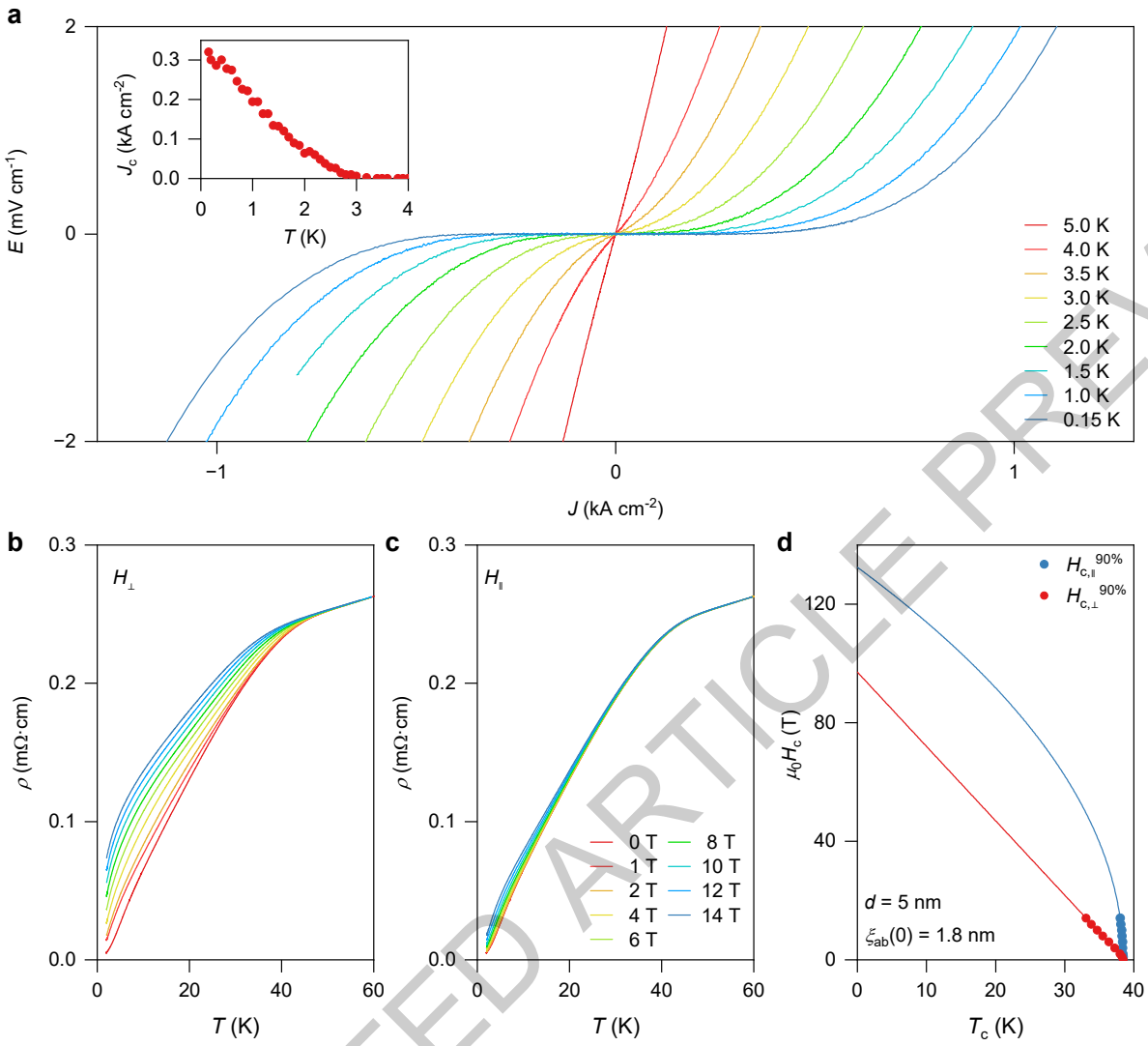

Figure 3, *E. K. Ko et al.*

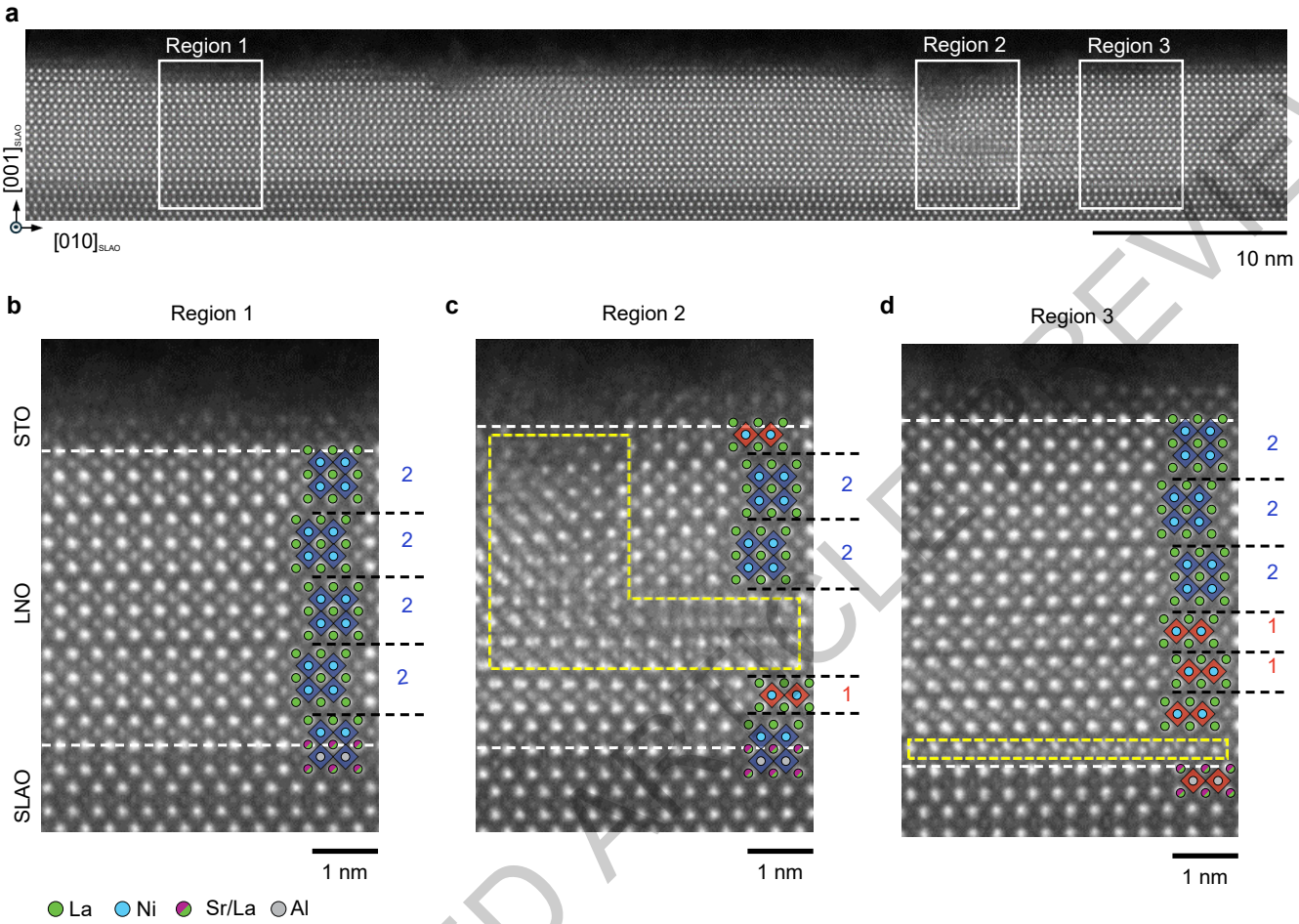

Figure 4, *E. K. Ko et al.*

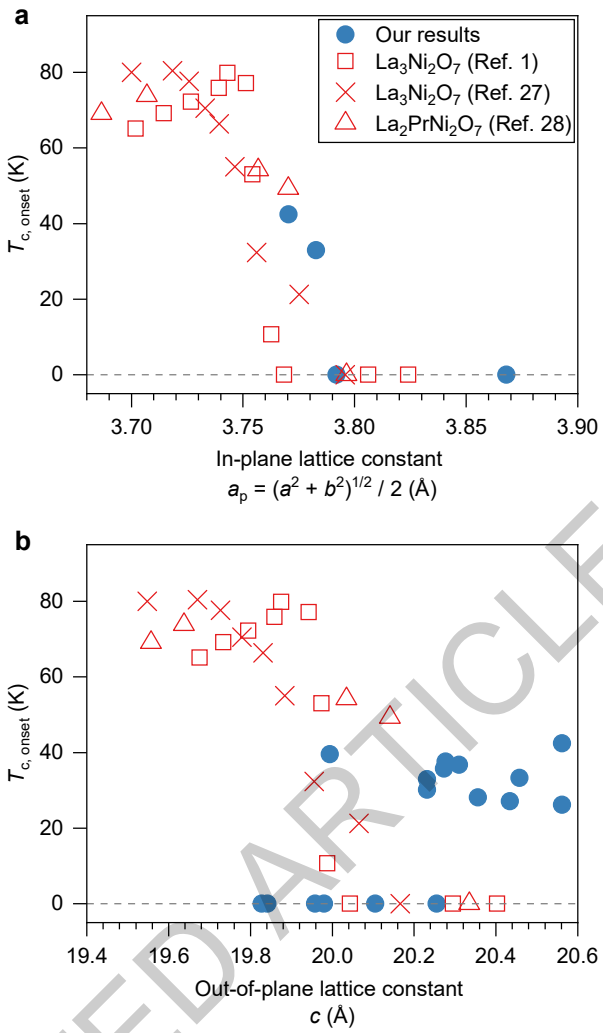

Figure 5, *E. K. Ko et al.*

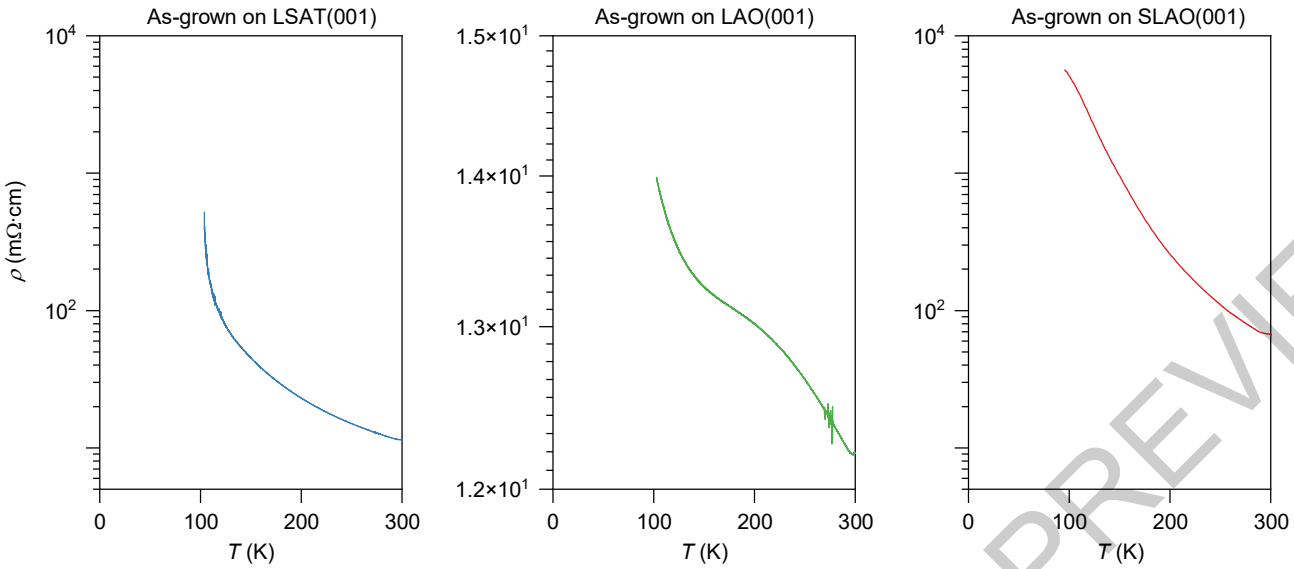

Extended Data Figure 1, *E. K. Ko et al.*

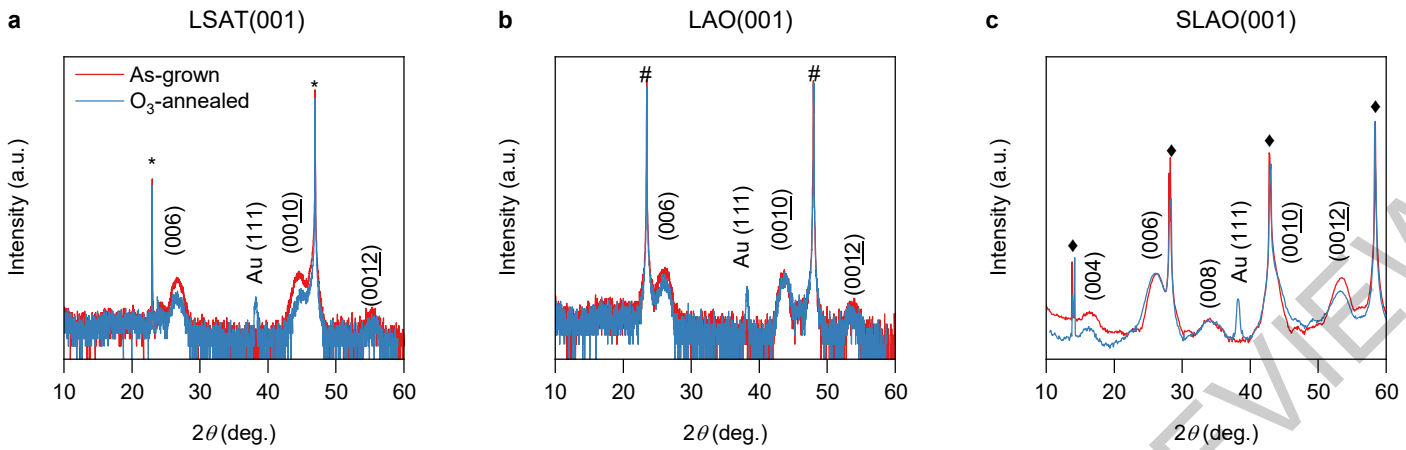

Extended Data Figure 2, *E. K. Ko et al.*

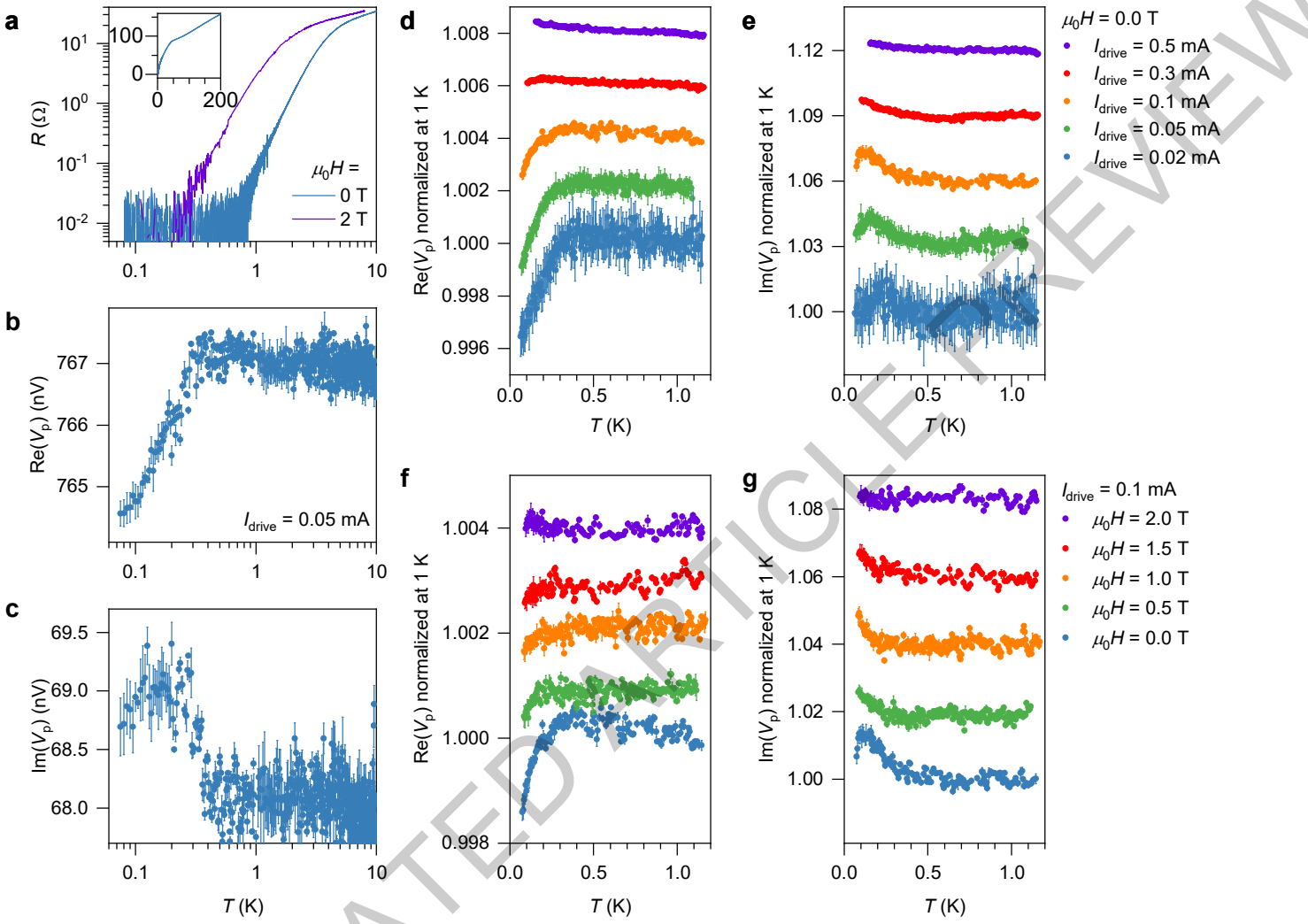

Extended Data Figure 3, *E. K. Ko et al.*

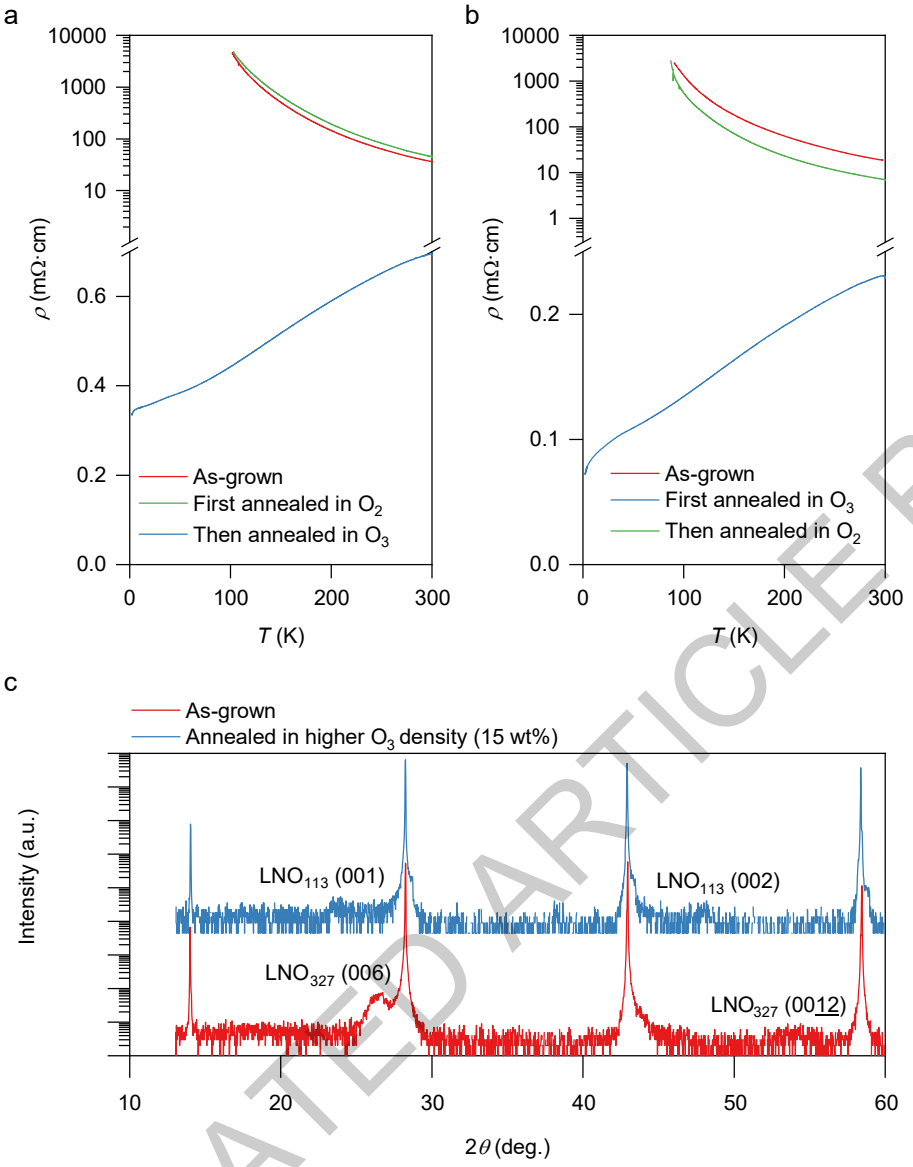

Extended Data Figure 4, *E. K. Ko et al.*

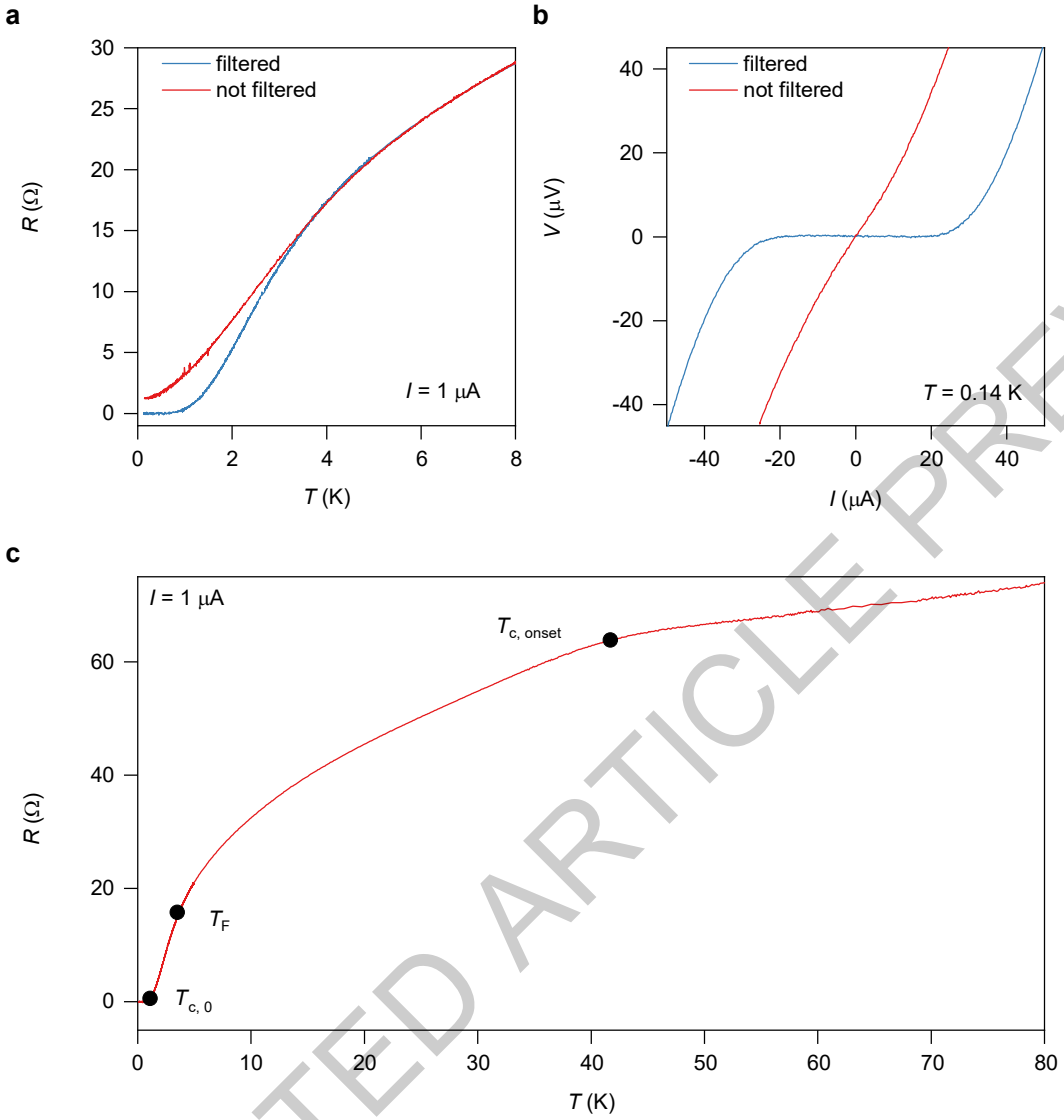

Extended Data Figure 5, *E. K. Ko et al.*

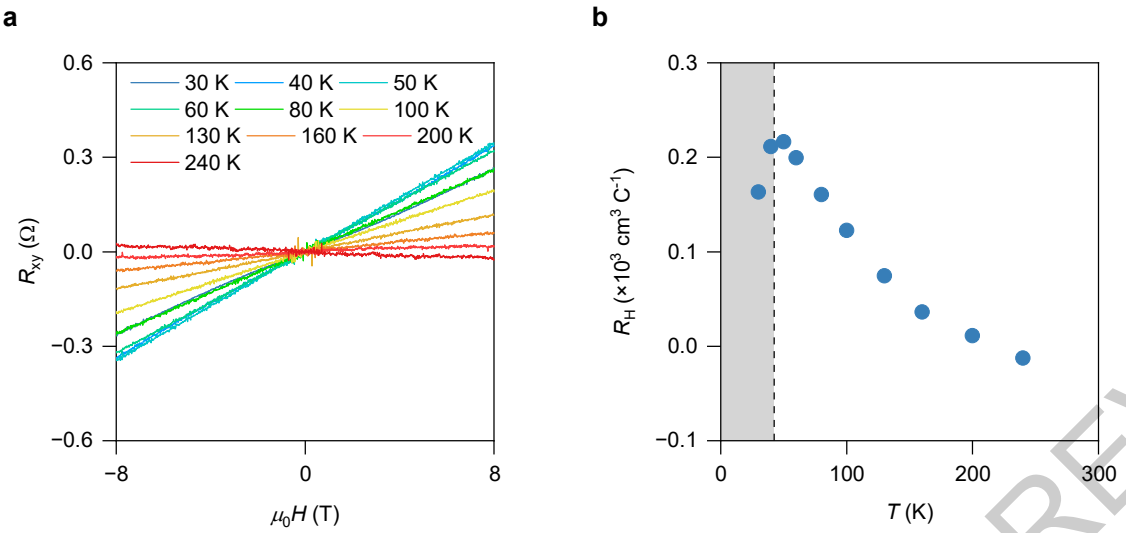

Extended Data Figure 6, *E. K. Ko et al.*

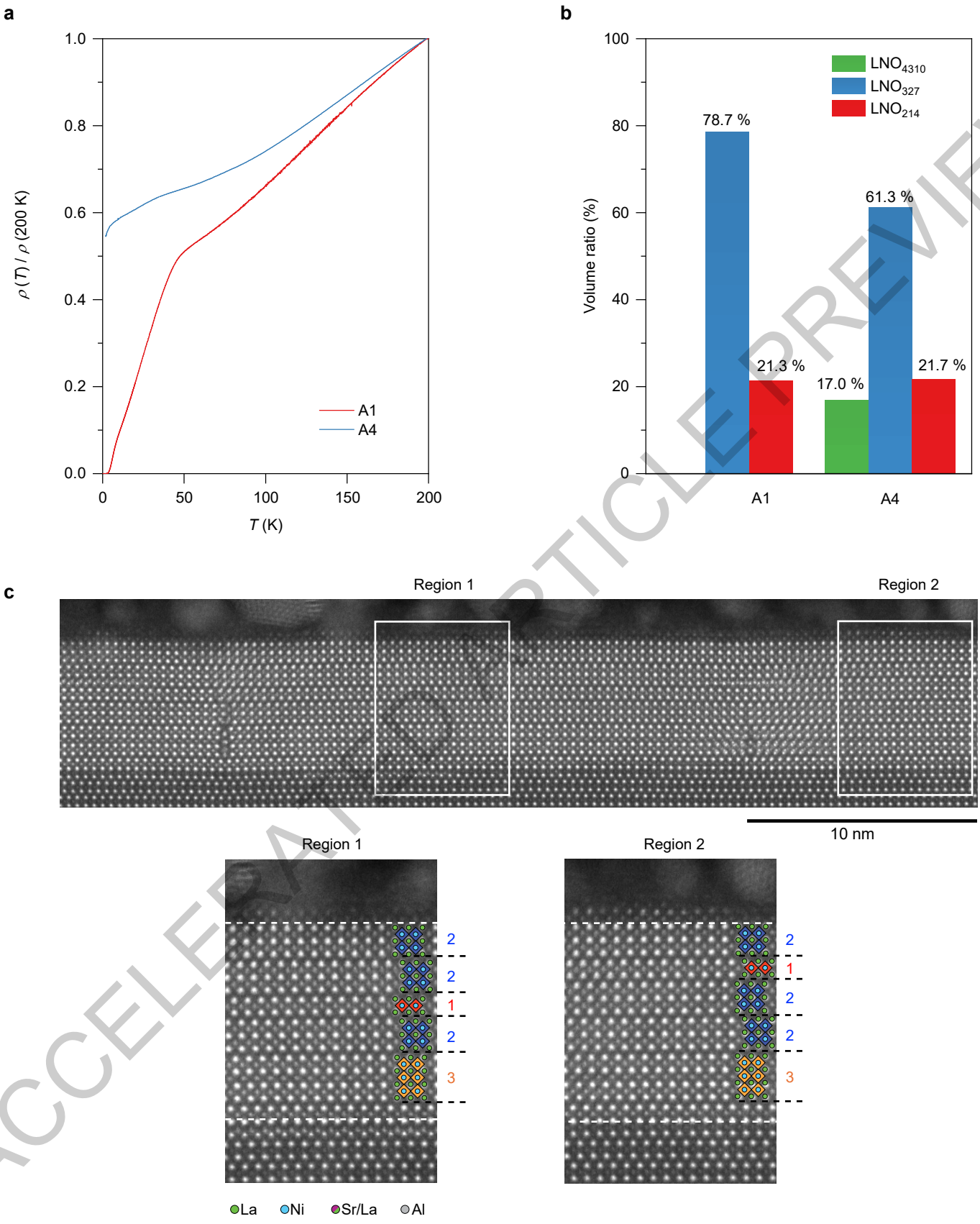

Extended Data Figure 7, *E. K. Ko et al.*

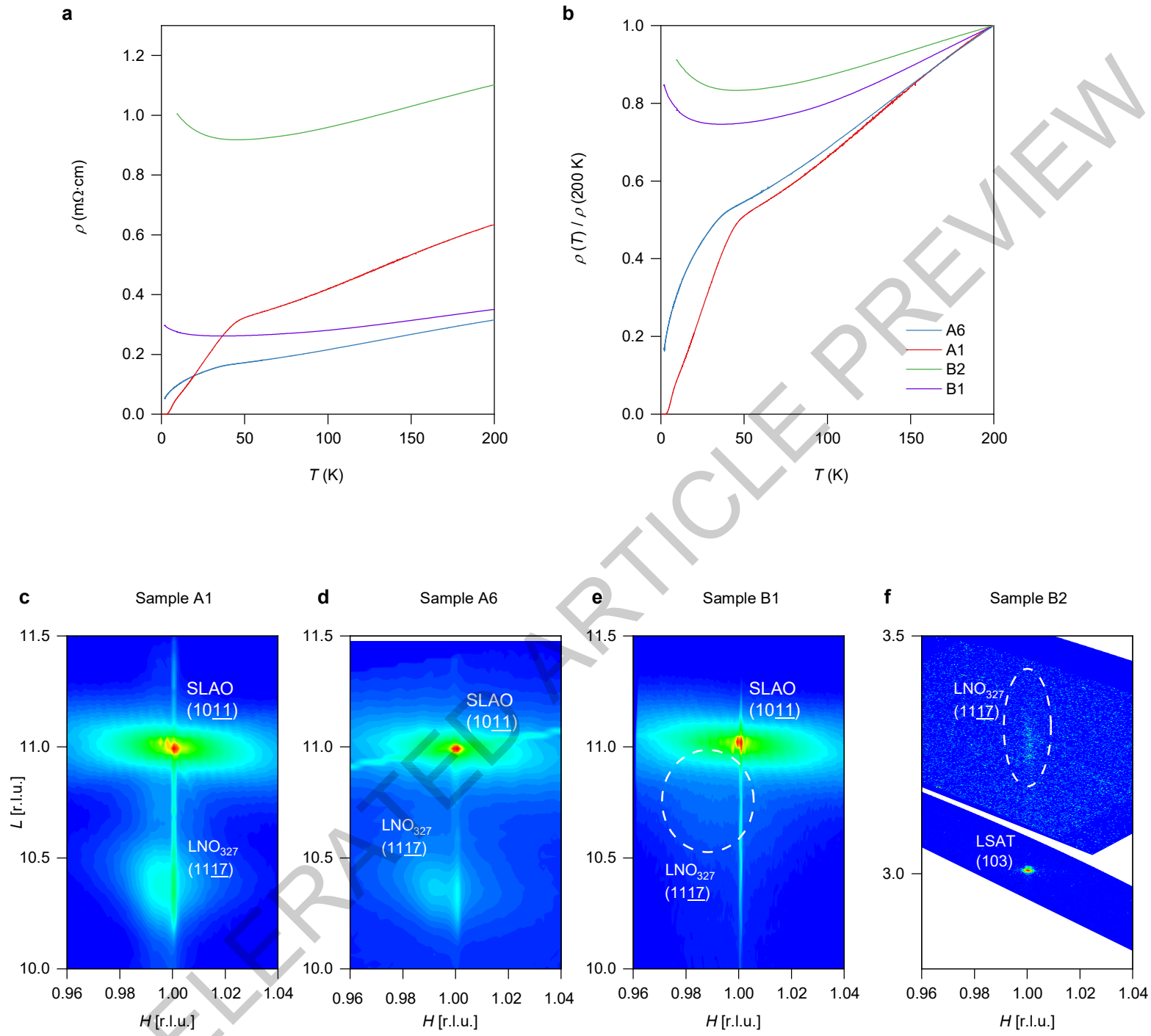

Extended Data Figure 8, *E. K. Ko et al.*

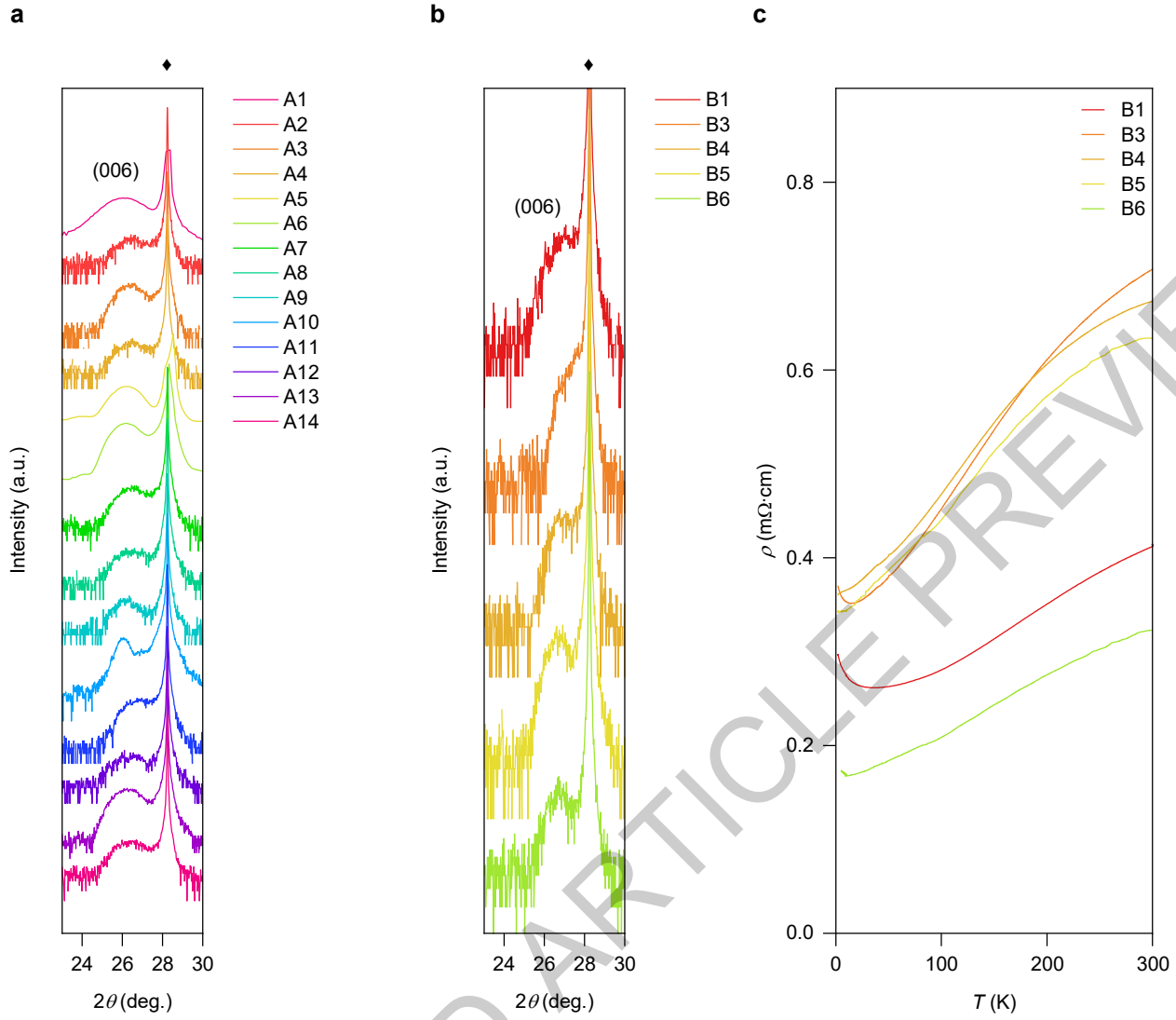

Extended Data Figure 9, *E. K. Ko et al.*

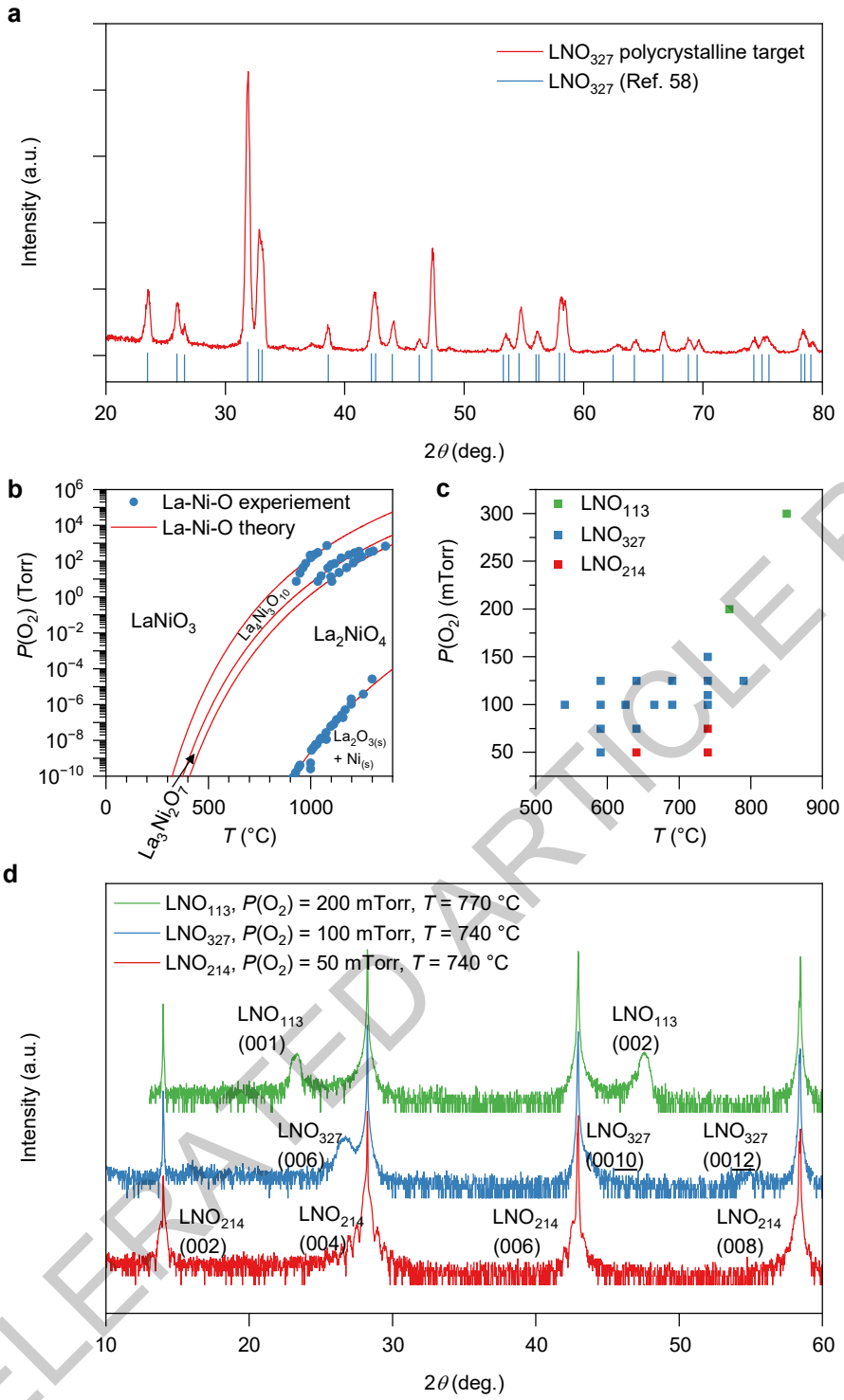

Extended Data Figure 10, *E. K. Ko et al.*